

Imaging through highly scattering human skulls with ultrasound-modulated optical tomography

YAN LIU,^{1,†}  RUIZHI CAO,^{1,†}  JIAN XU,¹  HAOWEN RUAN,^{1,2} AND CHANGHUEI YANG^{1,*}

¹Department of Electrical Engineering, California Institute of Technology, 1200 East California Boulevard, Pasadena, California 91125, USA

²Kernel LLC, Los Angeles, California 90036, USA

*Corresponding author: chyang@caltech.edu

Received 10 March 2020; revised 14 April 2020; accepted 20 April 2020; posted 21 April 2020 (Doc. ID 390920); published 20 May 2020

Advances in human brain imaging technologies are critical to understanding how the brain works and the diagnosis of brain disorders. Existing technologies have different drawbacks, and the human skull poses a great challenge for pure optical and ultrasound imaging technologies. Here we demonstrate the feasibility of using ultrasound-modulated optical tomography, a hybrid technology that combines both light and sound, to image through human skulls. Single-shot off-axis holography was used to measure the field of the ultrasonically tagged light. This Letter paves the way for imaging the brain noninvasively through the skull, with optical contrast and a higher spatial resolution than that of diffuse optical tomography. © 2020 Optical Society of America

<https://doi.org/10.1364/OL.390920>

Advances in human brain imaging technologies are critical to understanding how the brain works and the diagnosis of brain diseases. Magnetic resonance imaging (MRI) is the most widely used approach in functional brain imaging. However, the equipment is costly and non-portable and it cannot image subjects with implanted metal or electronic devices (for example, pacemakers). Positron emission tomography is also costly and non-portable; more importantly, it uses ionizing radiation. Pure optical imaging technologies do not have the aforementioned drawbacks, but they suffer from the poor spatial resolution caused by the scattering of light in biological tissue [1,2]. Compared to photons, ultrasound is much less scattered in tissue, but when it is used for brain imaging, ultrasound is attenuated and distorted by the round-trip propagation through the skull. Therefore, ultrasonography is suited for use in pediatric brain imaging before fontanelles close. However, its use in adult human brain imaging remains challenging. In addition, the primary contrast mechanism in ultrasound imaging is acoustic impedance contrast. Therefore, it cannot be used to collect biochemical information, and the low acoustic impedance contrast of soft tissue further limits the specificity.

Hence, hybrid technologies that use both light and sound such as photoacoustic tomography (PAT) [3] and ultrasound-modulated optical tomography (UOT) [4–6], have been regarded as potentially promising modalities for adult human brain imaging. They combine the advantage of functional

molecular (e.g., hemoglobin) contrast provided by optical imaging with the advantage of minimal tissue scattering by ultrasound. In addition, the ultrasonic wave transmits through the skull only once in these methods as opposed to twice in ultrasound imaging. Therefore, the signal should be less attenuated and distorted than the echo signal in ultrasonography.

While PAT through *ex vivo* monkey and human skulls has been demonstrated [7,8], UOT (or acousto-optic imaging) through human skulls has not been reported. In UOT, light passing through an ultrasonic focus undergoes a frequency shift by multiples of the ultrasonic frequency [9]. By detecting the frequency-shifted light (i.e., ultrasonically tagged light) as a function of the ultrasonic focus position, ultrasound defined resolution can be achieved in UOT [10–16].

As UOT is fundamentally different from PAT in the way ultrasound and light interacts, the impact of measurement parameters on the detectable signal level and resolution can differ for the two methods. Unlike PAT, which is sensitive mainly to the optical absorption property of tissue, UOT is sensitive to both the optical absorption and scattering properties [17]. Therefore, the UOT signal or signal change can potentially monitor a larger range of physiological changes in the human brain. Specifically, UOT can potentially measure blood oxygenation changes in the brain by using the spectral differences between oxygenated and deoxygenated blood (absorption contrast). UOT can also potentially measure blood perfusion changes by honing in on the scattering changes as the relative volume of the blood flowing through a brain region changes (scattering contrast). Additionally, a numerical simulation study has shown that one type of UOT, based on spectral hole burning (SHB), has the potential to achieve a larger imaging depth in human bodies compared with PAT [18]. One caveat is that SHB experiments require expensive, non-portable, and cumbersome equipment such as cryostats.

In this Letter, we demonstrate for the first time, to the best of our knowledge, imaging through highly scattering human skulls with UOT. Our method does not require cryogenic cooling and has the potential to be implemented as a head-mountable device. We used a single-shot off-axis holography method [19] to detect the UOT signal which, to the best of our knowledge, has not been demonstrated in the UOT field. The large pixel count of a camera enables parallel detection of multiple speckle grains within a single shot, which is crucial for this type of

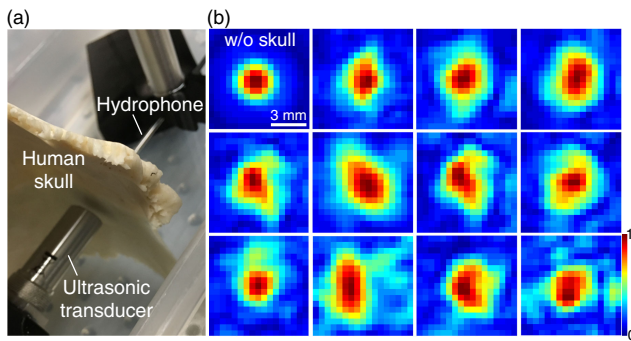


Fig. 1. Measuring the ultrasonic field distribution on the focal plane of a spherically focused transducer, with and without the presence of a human skull. (a) Photo of the experimental setup. (b) Normalized ultrasonic field distribution on the focal plane measured at different locations with respect to the fixed human skull. Note that the bone thickness is not uniform across the skull.

application where the signal-to-noise ratio (SNR) is low, and the speckle decorrelates rapidly due to physiological motions such as blood flow [20–22]. In previous work [23], multiple frames were recorded to reconstruct the UOT signal, making the method vulnerable to the rapid speckle decorrelation in living tissue. Single-frame UOT measurements have previously been reported [24–27]. However, some methods require special lock-in cameras in which each pixel is an analog lock-in detector [25–28]. Although off-axis holography has been used in heterodyne holography-based UOT, multiple frames were required to filter out the local oscillator beam [29].

In our experiments, we first evaluated the extent by which a human skull distorts the ultrasonic field. A hydrophone (HNR-0500, ONDA) was used to measure the ultrasonic field distribution on the focal plane of a spherically focused single-element ultrasonic transducer (A303S, Olympus; central frequency = 1 MHz, focal length = 15.2 mm, element diameter = 12.7 mm) with and without the presence of a human skull (3–5 mm thick, human parietal bone, SHN-46, Skulls Unlimited International Inc.). Figure 1(a) shows a photo of the setup, and Fig. 1(b) shows the normalized ultrasonic field distribution. The full width at half-maximum (FWHM) focal spot size was measured to be 3 mm when the skull was absent. When the skull was present between the transducer and the hydrophone, depending on the location of the ultrasonic transducer relative to the skull, the FWHM focal spot size varied from 3 mm to 6 mm, and the ultrasonic pressure at the focus was attenuated to 10–20%. Although the focus was distorted and broadened, we observed that it was still achievable through the human skull for 1 MHz ultrasound—a result that is consistent with previous literature findings [30].

Next, we built a camera-based UOT system (schematically shown in Fig. 2) to demonstrate the feasibility of imaging an absorptive object buried between two pieces of highly scattering human skull. The output of a continuous-wave (cw) laser (671 nm, MSL-FN-671-S, CNI Optoelectronics Tech Co.; ~35 mW on the sample) passed through an optical isolator, a variable attenuator composed of a half-wave plate (HWP1), and a polarizing beam splitter (PBS1), before it was split into a reference beam (R) and a sample beam (S) by a polarizing beam splitter (PBS2). After passing through a neutral density (ND) filter, the reference beam was expanded to a diameter of

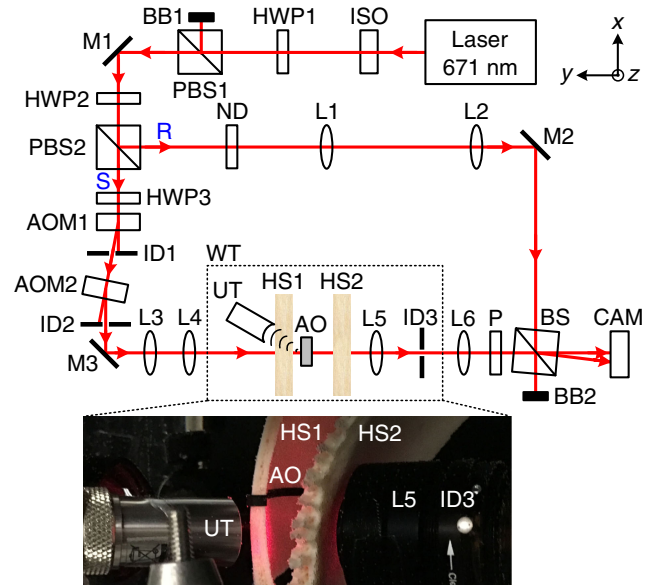


Fig. 2. Schematic of the UOT setup for imaging through highly scattering human skulls. AO, absorptive object; AOM, acousto-optic modulator; BB, beam block; BS, non-polarizing beam splitter (90% transmission, 10% reflection); CAM, camera; HWP, half-wave plate; HS, human skull; ID, iris diaphragm; ISO, isolator; L, lens; M, mirror; ND, neutral density filter; P, polarizer; PBS, polarizing beam splitter; R, reference beam; S, sample beam; UT, ultrasonic transducer; WT, water tank. The components in the water tank are enclosed in a dashed box, and a photo is shown.

1" by two lenses (L1 and L2), and reflected by a 90:10 (T:R) non-polarizing beam splitter (BS) before it illuminated a camera sensor. The sample beam passed through a half-wave plate (HWP3), two acousto-optic modulators (AOM1 and AOM2, which shifted the frequency of the sample beam by 50 MHz and -49 MHz sequentially), and a beam expander, before it illuminated the human skulls. An ultrasonic transducer focused 1 MHz ultrasound through the skull, and the focal pressure amplitude is ~ 0.34 MPa. A portion of the light passing through the ultrasonic focus was tagged by the ultrasound, and its frequency was shifted to the same frequency as the reference beam. The ultrasonically tagged light and untagged light passed through an absorptive object (a strip of 2 mm wide and 3 cm long black tape, transmittance $< 0.1\%$, attached on the skull), a second human skull (1.5 cm away from the first skull), a $4f$ system (with an iris in the pupil plane to adjust the speckle size), a polarizer, and the BS before they interfered with the reference beam ($\sim 45^\circ$ with respect to the x and z axes) and detected by a camera (pco.edge 5.5, PCO-TECH; global shutter, 2560×2160 pixels, $6.5 \mu\text{m}$ pixel size). Because the ultrasonically tagged light had the same frequency as that of the reference beam, its interference pattern was stable on the camera. In contrast, the interference pattern formed by the untagged light and the reference beam was a 1 MHz beat, and thus was averaged out during the camera exposure time (5 ms).

To reconstruct the field of the ultrasonically tagged light, we first took the two-dimensional (2D) Fourier transform of the recorded interferogram. An example of the resulting spectrum is shown in Fig. 3(a). The two faint circles along the 45° diagonal are the spectra corresponding to the interference pattern

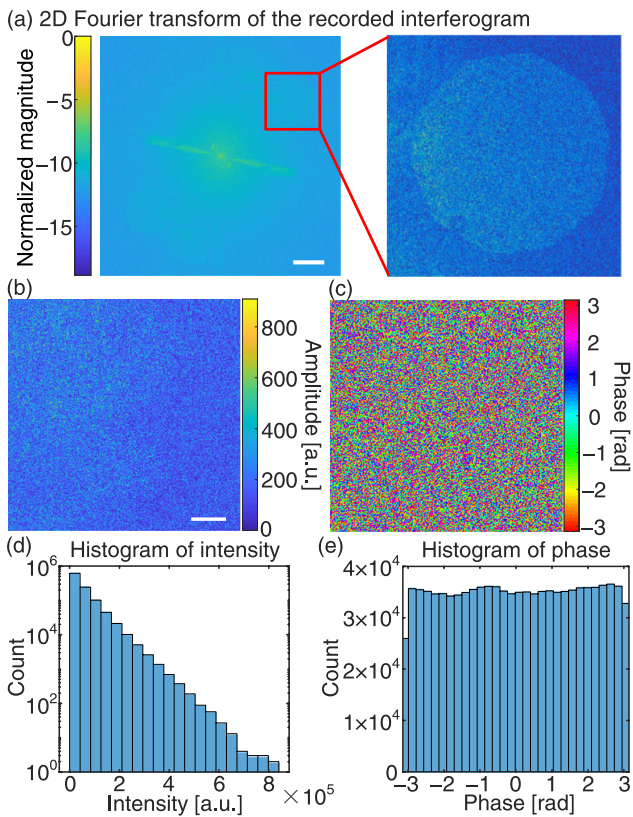


Fig. 3. Reconstruction of the field of the ultrasonically tagged light from the single-shot off-axis hologram. (a) 2D Fourier transform of the recorded interferogram. The normalized magnitude is plotted in a log scale. A close-up of the sideband is shown on the right. Scale bar, 20 cycles/mm. (b) Amplitude of the reconstructed ultrasonically tagged light field. Scale bar, 1 mm. (c) Phase of the reconstructed ultrasonically tagged light field. (d) Histogram of intensity. (e) Histogram of phase.

between the ultrasonically tagged light and the reference beam. A close-up of one of the spectra is shown on the right. To obtain the field of the ultrasonically tagged light, we cropped one of the sidebands, shifted it to the center of the Fourier space, and performed 2D inverse Fourier transform. The resulting amplitude and phase of the reconstructed ultrasonically tagged light field is shown in Figs. 3(b) and 3(c), respectively. Because the skulls are highly scattering, we expect the speckle field to be fully developed. Indeed, from the histogram of intensity shown in Fig. 3(d) and the histogram of phase shown in Fig. 3(e), we find that the intensity of ultrasonically tagged light roughly follows the exponential distribution, and the phase roughly follows the uniform distribution, which are characteristics of fully developed speckles. We obtained the UOT signal by summing up the energy of the ultrasonically tagged light over all the pixels within the reconstructed image.

To obtain an image of the absorptive object, we scanned the ultrasonic focus with respect to the object along the x direction (see the labeling of axes in Fig. 2) and measured the UOT signal at each scanning position. By plotting the normalized UOT signal as a function of the ultrasonic focus position, we obtained an image of the object, which is shown in the blue solid curve in Fig. 4. The dip of the curve at ~ 6 mm position manifests the object, because the object absorbed some of the light. When we removed the object and repeated the measurement (see the red

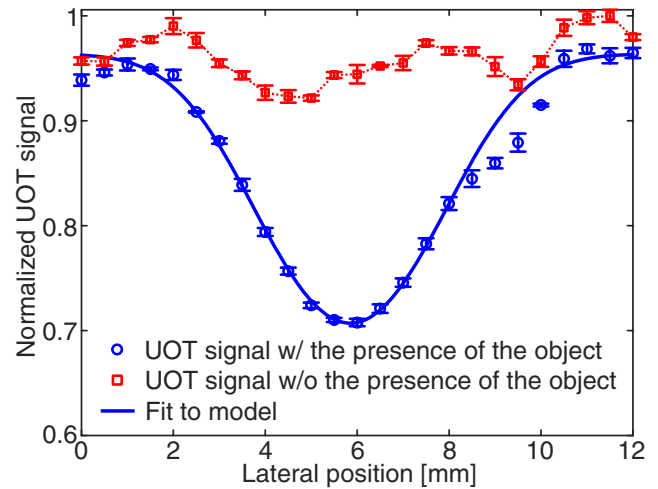


Fig. 4. UOT signal as a function of the ultrasonic focus position with (blue circles) and without (red squares) the presence of an absorptive object. The blue solid curve denotes the fitting to the experimental data with the model shown in Eq. (1). Each data point is an average of four measurements. The error bar represents the standard deviation.

dotted curve in Fig. 4), we did not observe a similar dip, and the curve is relatively flat, showing that the image contrast in the blue solid curve is mainly caused by the object, rather than the skull inhomogeneity.

Assuming that the imaging system is linear and shift invariant, the image can be theoretically computed by

$$I(\vec{r}) = o(\vec{r}) * h(\vec{r}), \quad (1)$$

where $*$ denotes convolution; $o(\vec{r})$ describes the object and can be modeled by a rectangular function with a width of 2 mm; $h(\vec{r})$ is the 1D point spread function (PSF) of the system and is determined by the ultrasonic focal intensity profile. $h(\vec{r})$ can be modeled by a Gaussian function with a FWHM size related to the system lateral resolution determined by the ultrasonic frequency, numerical aperture, and skull distortion. By fitting the experimental data with the imaging model [25] (see the blue solid curve in Fig. 4), the FWHM lateral resolution is found to be 3.4 mm, which is within the normal range considering the skull induced distortion of the PSF. Misalignment of the ultrasonic focus position with respect to the object along the y direction also degrades the measured lateral resolution.

In this Letter, we use a hybrid technology combining light and sound to image through highly scattering human skulls. Our method images optical contrast at depths with ultrasound resolution. Therefore, it can achieve a higher spatial resolution than that of diffuse optical tomography [20]. Currently, the resolution along the acoustic axis direction is poor, because we used a cw laser (and thus a long burst of ultrasound) in this experiment. The axial resolution can be improved by using a pulsed laser and a single cycle of ultrasonic pulse [31]. This can also improve the lateral resolution and image contrast, because the tagging volume is much bigger in the cw case, and the beam widths at out-of-focus planes are larger than that at the focal plane.

In our experiment, we used a single-element transducer to generate an ultrasonic focus through the human skull. Better focusing quality (e.g., smaller focal spot and higher focus to

background pressure ratio) can be achieved with a high numerical aperture transducer array and acoustic wavefront shaping to correct for the skull induced aberration (i.e., adjusting the delay of each element to let the fields associated with different elements constructively interfere at the focus) [32]. Due to the reciprocity of acoustic waves, PAT in theory can achieve the same spatial resolution through the skull as UOT. It would require PAT methods to correctly find the delay of each transducer element. One way to find such delays in PAT would be to use a computational model which incorporates the skull morphology and composition information obtained from x-ray computed tomography (XCT) [7]. However, the effectiveness of this method relies on precise registration of the two imaging modalities involved (i.e., XCT and PAT) and the accuracy of the skull model. While this method works well for monkey skulls [7], its effectiveness for adult human skulls remains to be demonstrated experimentally. In comparison, it may potentially be easier to find such delays experimentally in UOT experiments. For example, one can adjust the delay of each element until the nonlinear UOT signal or the temperature rise at a target location monitored by MRI is maximized [33]. In such UOT experiments, we would also avoid the need to perform registration with XCT—another source of error in PAT.

We demonstrate the feasibility of imaging an object through human skulls using a transmission-mode system. Because human frontal bones and parietal bones are highly curved, our experiment mimics the case where we illuminate from one location of the bone and detect the transmitted light at an offset location from the illumination site. For other non-curved bones, a reflection-mode system should be used.

The speckle size on the camera and the angle of the reference beam should be controlled so that the sideband in the Fourier space does not overlap with the zeroth order, while the area of the sideband should be maximized to capture more speckles to increase the signal. The speckle size on the camera was 5.6 pixels wide in our experiment, and it can be further reduced to 4 pixels wide to increase the signal [34]. In addition, rather than using a circular iris, a rectangular iris can be employed to maximally use the Fourier space in off-axis holography [29].

The off-axis holography-based UOT detection method has a high sensitivity. Because interferometry is used to boost the signal above the detector noise, the detection is shot-noise limited. The expression of the SNR can be derived and written as

$$\text{SNR}_{\text{cam}} = \frac{\text{UOT signal}}{\sqrt{\text{Var}(\text{UOT signal})}} = \frac{\sqrt{N_p} \bar{N}_T}{\sqrt{4\bar{N}_T + 1}}, \quad (2)$$

where \bar{N}_T is the average number of ultrasonically tagged photons per pixel; N_p is the pixel count of the camera. In deriving Eq. (2), we assumed that the number of reference beam photons per pixel equals the average number of untagged photons per pixel, and both numbers are much larger than \bar{N}_T , which is commonly achieved in experiments; we also assumed a quantum efficiency of 1 and a rectangular iris is employed. Assuming $N_p = 10^6$, Eq. (2) shows that the SNR is above one as long as $\bar{N}_T > 1/\sqrt{N_p} = 10^{-3}$.

Funding. Kernel–Brain Research and Technologies (FS 13520230).

Acknowledgment. The authors thank Haojiang Zhou, Michelle Cua, Joshua Brake, Jamu Alford, and Adam Marblestone for discussions.

Disclosures. C. Yang: (F, P). Other authors declare no conflicts of interest.

†These authors contributed equally to this Letter.

REFERENCES

- V. Ntziachristos, *Nat. Meth.* **7**, 603 (2010).
- Y. Liu, C. Zhang, and L. V. Wang, *J. Biomed. Opt.* **17**, 126014 (2012).
- L. V. Wang and S. Hu, *Science* **335**, 1458 (2012).
- D. S. Elson, R. Li, C. Dunsby, R. Eckersley, and M.-X. Tang, *Interface Focus* **1**, 632 (2011).
- S. G. Resink, A. C. Boccara, and W. Steenbergen, *J. Biomed. Opt.* **17**, 040901 (2012).
- J. Gunther and S. Andersson-Engels, *Front. Optoelectron.* **10**, 211 (2017).
- C. Huang, L. Nie, R. Schoonover, Z. Guo, C. Schirra, M. Anastasio, and L. Wang, *J. Biomed. Opt.* **17**, 066016 (2012).
- L. Nie, X. Cai, K. Maslov, A. Garcia-Urbe, M. Anastasio, and L. Wang, *J. Biomed. Opt.* **17**, 110506 (2012).
- Y. Huang, M. Cua, J. Brake, Y. Liu, and C. Yang, *J. Biomed. Opt.* **25**, 025002 (2020).
- L. Wang and X. Zhao, *Appl. Opt.* **36**, 7277 (1997).
- F. Ramaz, B. Forget, M. Atlan, A. C. Boccara, M. Gross, P. Delaye, and G. Roosen, *Opt. Express* **12**, 5469 (2004).
- M. Atlan, B. C. Forget, F. Ramaz, A. C. Boccara, and M. Gross, *Opt. Lett.* **30**, 1360 (2005).
- S. Farahi, G. Montemezzani, A. A. Grabar, J.-P. Huignard, and F. Ramaz, *Opt. Lett.* **35**, 1798 (2010).
- H. Zhang, M. Sabooni, L. Rippe, C. Kim, S. Kröll, L. V. Wang, and P. R. Hemmer, *Appl. Phys. Lett.* **100**, 131102 (2012).
- P. Lai, X. Xu, and L. V. Wang, *J. Biomed. Opt.* **17**, 066006 (2012).
- S. G. Resink, E. Hondebrink, and W. Steenbergen, *Opt. Express* **22**, 3564 (2014).
- S.-R. Kothapalli, S. Sakadzic, C. Kim, and L. V. Wang, *Opt. Lett.* **32**, 2351 (2007).
- A. Walther, L. Rippe, L. V. Wang, S. Andersson-Engels, and S. Kröll, *Biomed. Opt. Express* **8**, 4523 (2017).
- E. Cuche, P. Marquet, and C. Depeursinge, *Appl. Opt.* **39**, 4070 (2000).
- T. Durduran, R. Choe, W. B. Baker, and A. G. Yodh, *Rep. Prog. Phys.* **73**, 076701 (2010).
- M. M. Qureshi, J. Brake, H.-J. Jeon, H. Ruan, Y. Liu, A. M. Safi, T. J. Eom, C. Yang, and E. Chung, *Biomed. Opt. Express* **8**, 4855 (2017).
- Y. Liu, P. Lai, C. Ma, X. Xu, A. A. Grabar, and L. V. Wang, *Nat. Commun.* **6**, 5904 (2015).
- S. Lévêque, A. C. Boccara, M. Lebec, and H. Saint-Jalmes, *Opt. Lett.* **24**, 181 (1999).
- J. Li, G. Ku, and L. V. Wang, *Appl. Opt.* **41**, 6030 (2002).
- Y. Liu, Y. Shen, C. Ma, J. Shi, and L. V. Wang, *Appl. Phys. Lett.* **108**, 231106 (2016).
- K. Barjean, K. Contreras, J.-B. Laudereau, É. Tinet, D. Etori, F. Ramaz, and J.-M. Tualle, *Opt. Lett.* **40**, 705 (2015).
- S. P. Morgan, C. Li, B. R. Hayes-Gill, N. B. E. Sawyer, and C. Kongsavatsak, *Proc. SPIE* **6086**, 608615 (2006).
- Y. Liu, C. Ma, Y. Shen, and L. V. Wang, *Opt. Lett.* **41**, 1321 (2016).
- M. Gross, P. Goy, and M. Al-Koussa, *Opt. Lett.* **28**, 2482 (2003).
- K. Hynynen and F. A. Jolesz, *Ultrasound Med. Biol.* **24**, 275 (1998).
- H. Ruan, J. Brake, J. E. Robinson, Y. Liu, M. Jang, C. Xiao, C. Zhou, V. Gradinaru, and C. Yang, *Sci. Adv.* **3**, eaao5520 (2017).
- J.-F. Aubry, M. Tanter, M. Pernot, J.-L. Thomas, and M. Fink, *J. Acoust. Soc. Am.* **113**, 84 (2003).
- D. Chauvet, L. Marsac, M. Pernot, A.-L. Boch, R. Guillevin, N. Salameh, L. Souris, L. Darrasse, M. Fink, M. Tanter, and J.-F. Aubry, *J. Neurosurg.* **118**, 1046 (2013).
- C. Ma, F. Zhou, Y. Liu, and L. V. Wang, *Optica* **2**, 869 (2015).